Comparative XRD analysis of PVA/TiO_2, PVA/ZrO_2 and $PVA/TiO_2/ZrO_2$ Composites

[1] Dr Jyotsna Chauhan,[2]akansha mehto, [3]Shaswat Chauhan

[1]Professor in RGPV,[2]Research scholar ,[3] BITS Pilani GOA

ABSTRACT: The present study investigated the doping effects of different phases of TiO_2 upon the PVA membranes structural, morphological, optical and photoluminescence characteristics. TiO_2 nanoparticles prepared by sol-gel technique and different phases successfully achieved by controlling calcination temperature. PVA/TiO_2 membranes were then fabricated by solution casting method. XRD studies confirmed the existence of different phases of TiO_2 nanoparticles in PVA. TEM results indicate that the TiO_2 nanoparticles size increased as the calcination temperature increased. The XRD spectrum also shows that doping enhances the crystallinity of polymer composites. The UV-visible spectra show decrease in optical energy band gap (Eg) with different phases of TiO_2 nanoparticles.. This indicates that PVA/TiO_2 (brookite) membrane has higher photocatalytic activity than the other two composite membranes. The enhanced properties of the PVA/TiO_2 composite membranes, which incorporate three distinct phases of TiO_2, offer benefits for a variety of applications.

[Dr Jyotsna Chauhan, akansha mehto, Shaswat Chauhan. Comparative XRD analysis of PVA/TiO_2, PVA/ZrO_2 and $PVA/TiO_2/ZrO_2$ Composites. *Rep Opinion* 2026;18(8):8-22]. ISSN 1553-9873 (print); ISSN 2375-7205 (online). http://www.sciencepub.net/report. 02. doi:10.7537/marsroj180826.02

Keywords: Comparative XRD; analysis; PVA/TiO_2; PVA/ZrO_2; $PVA/TiO_2/ZrO_2$ Composites

. The XRD results of the PVA/ZrO_2 composite sample reveal that ZrO_2 nanoparticles were successfully incorporated into PVA matrix and the crystallinity of composite increases with the addition of ZrO_2.
. Our study also indicates that these composites can be used for UV shielding materials, diodes and optoelectronic devices.
This comprises the outcomes of successful fabrication of PVA/TiO_2 and $PVA/TiO_2/ZrO_2$ composite membranes via solution casting technique. The TiO_2 and ZrO_2 nanoparticles are formed through the sol gel method. The benefits of addition of both TiO_2 and ZrO_2 nanoparticles together in PVA matrix have been studied using several characterization techniques.

The XRD results demonstrated the successful fabrication of PVA/TiO_2 and $PVA/TiO_2/ZrO_2$ nanocomposite membranes. These findings also highlight the enhanced crystallinity of the nanocomposites. Interestingly, it was noticed that $PVA/TiO_2/ZrO_2$ membrane exhibits a higher degree of crystallinity than that of PVA/TiO_2 membrane. The absorption study of composite membranes revealed a significant increase in absorbance intensity when moving from sample PVA to $PVA/TiO_2/ZrO_2$. Furthermore, notable shifts were observed in the positions of the absorbance peaks. These results illustrate the applications for different optical devices.

At room temperature, the composite membranes demonstrate photoluminescence and there has been a noticeable enhancement in the PL intensity of $PVA/TiO_2/ZrO_2$ composite as compared to PVA/TiO_2 composite, indicating its potential suitability for optoelectronic applications.

Introduction:

Refractory ceramics are defined as a material that maintain their physical and chemical stability even under conditions of elevated temperatures. Refractory ceramics fundamental thermophysical and thermomechanical characteristics are associated with its capacity to resist various degrees of mechanical and thermal stress, as well as prevent corrosion by both gases and liquids [3,4]. Generally, refractory oxides are resistant to abrupt temperature changes and also have characteristics render them well-suited for diverse applications [5]. These oxides are broadly categorized as refractory ceramics. There are a number of ceramic oxides which are good refractories because they are mechanically strong and have a high melting point. Ceramic refractories is non-metallic materials that can withstand high temperatures and used as insulating materials, blast furnace linings and other high-temperature applications. There is a large variety of ceramic refractories that can be categorized using various criteria. Ceramic refractories are categorized into three general types based on their chemical composition: oxide refractories, non-

oxide refractories and mixtures of both, known as composite refractories [6,7].
The diverse uses of polymer nanocomposites in packaging of food, coatings, air and water purification, batteries and solar cells have led to substantial research into these materials [1-4]. Among the different polymer polyvinyl alcohol (PVA) focused much attention as result of its distinctive qualities, like environment friendly, solubility in water, non-toxic, biodegradable, excellent optical and electrical properties, charge storage capability and chemical stability [5-8]. Several studies show the different applications of PVA when tuned its optical and structural properties by doping [9-13]. The OH group in PVA is responsible for majority of the physical properties that gives rise to the substances wide range of industrial uses [14].

Nanocomposites made of an organic polymer and inorganic material are gaining a much attention because of their outstanding properties and numerous uses [15-17]. The fabrication of inorganic and organic hybrid systems devices like optoelectronic devices, solar cell and photoelectrode can result in the invention of novel devices technologies [18-20]. Polymer/ceramic oxide composites have also received a lot of research attention for the separator of supercapacitors [21, 22]. Lithium-ion batteries are promising alternatives for portable gadgets and electric cars because of its small size, cheap maintenance, extended life cycle and higher energy density [23]. However, increasing the lithium-ion batteries use into novel energy storage devices with low self-discharge requires improved battery safety [24-26]. Yanilmaz et al. reported separators play a crucial role to prevent short circuits through restricting physical connection between electrodes. Simultaneously, allowing the movement of lithium-ions between them during cycles of charging and discharging. The
separators must have appropriate pore size, exceptional thermal and chemical stability, sufficient thickness and superior permeability to lithium-ions. [27].

Xiao et al. reported that PVA serves a famous as a superior material for membranes because of its exceptional qualities including good film-forming ability and superior mechanical, chemical, and thermal stabilities. Numerous investigations have been conducted since the introduction of membranes based on PVA as separators in diverse fuel cells. PVA, a crucial component of the gel electrolyte in microbial fuel batteries, has generated a lot of interest [28]. Doping of inorganic ceramic oxide nanoparticles can enhance characteristics of PVA membranes. It has been discovered that doping of ceramics oxides to the polymer matrix increases ionic conductivity because they add porosity to the PVA matrix by expanding the amorphous areas of the crystalline polymer [29]. According to studies, incorporating inorganic particles into separator membranes is a good strategy to increase thermal stability and electrochemical performance [30-33].

A lot of interest has been paid to titanium dioxide (TiO_2) because of its promising qualities. It is an inorganic semiconductor with a large band gap that finds extensive use in various fields, such as air and water purification, photocatalysis, sensors and self-cleaning windows [34]. Anatase, brookite and rutile is the three main phases of TiO_2. The utmost stable phase of TiO_2 was discovered to be rutile, while the other two (anatase and brookite) are metastable forms [35, 36]. When TiO_2 and PVA polymer are combined, they may interact in the polymers crystalline or amorphous regions, changing its electrical, structural and optical characteristics [37].

Gupta et al. reported the ball milling process for the preparation of TiO_2 nanoparticles in order to increase the photocatalytic activity and mechanical strength and suggest that by optimizing the rotating speed, ball to grinding material ratio and grinding time the desired properties of grinding material may be tuned [38]. Ramakrishnan et al. investigated solvothermal and microwave techniques to produce TiO_2 nanoparticles for use in dye-sensitized solar cells

2.1. *Experimental Technique:*

2.1.1. Preparation method of TiO_2 nanoparticles:

The TiO_2 nanoparticles organized via the sol gel method. We first prepared the ethanol and methanol solution and then TTIP add in the solution with continuously stirring. HCl drops were included to stabilize the pH of mixture between 2 to 3 and continued to stirring for next three hours. Then the reaction was stopped by adding water and stirred again as long as 2 hours using a magnetic stirrer. After three days of ageing, the sample dried to 85 °C on a hot plate and it was then grinding for 30 minutes. To obtain different phases of TiO_2,

the sample was calcined to 300°C for the brookite, 600°C for the brookite-rutile and 1000°C for the rutile phase.

2.1.2. Preparation method of ZrO_2 nanoparticles:

We used sol-gel method to synthesized ZrO_2 nanoparticles. To produce ZrO_2 nanoparticles, 0.058M of zirconium acetate hydroxide add into 100 ml of distilled water with continuously stirring to 30 minutes utilizing a magnetic stirrer and thereafter slowly added NH_4OH solution to maintain the pH of solution 7-8. The solution was left overnight at ambient temperature with continuously stirring to enhance aging and then centrifuged in order to extract water. Water and ethanol were used for rinsing the sample after that filter paper was used for the filtration of gel. The obtained gel subsequently dried around 70°C temperature after which it was broken into small particles by grinding and calcined for 2 hours around 650 °C to produce ZrO_2 nanoparticles.

2.1.3. Synthesis of PVA, PVA/TiO_2, PVA/ZrO_2 and PVA/ TiO_2/ZrO_2 composite membranes:

2.1.3.1. Preparation of pure PVA membranes:

To prepare PVA membranes, PVA solution was prepared through dissolution of 1 gm PVA in 20 ml distilled water subsequently stirred it at 80°C while it turned transparent. Following put this solution to a Petri dish, the mixture was permitted to dry at ambient temperature, after that, dried film removed from Petri dish and resulting in a transparent PVA membrane.

2.1.3.2. Preparation of PVA/TiO_2 composite membranes:

Solution casting technique was utilized to produce PVA/TiO_2 composite membrane. To prepare TiO_2 solution, 0.05 grams of TiO_2 nanoparticles were mixed in distilled water of 10 ml and sonicated for 1 hour. At the same time, PVA solutions were prepared by dissolving 1 gm of PVA into 20 ml of distilled water and stirred at 80°C until it reached a transparent state. The prepared TiO_2 solution were combined with the PVA solutions and the resulting mixture was then sonicated for two hours to achieve homogeneous dispersion of TiO_2 nanoparticles within the PVA. The obtained solution was poured into Petri dish and allowed to dry at room temperature for 2 days. After that, the dried films were removed. The same process is also repeated for the preparation of PVA/TiO_2 membrane with various TiO_2 phases (brookite, brookite-rutile and rutile).

2.1.3.3. Preparation of PVA/ZrO_2 composite membranes:

We prepared PVA/ZrO_2 nanocomposite membranes with various loading of ZrO_2 nanoparticles (5 wt%, 9 wt% and 13 wt%). A pure and homogenous PVA solution was prepared by dissolving 1 gm of PVA in 20 ml distilled water and stirred at 80°C until a transparent solution was obtained. Simultaneously, ZrO_2 nanoparticles (5 wt%) were separately dispersed in 10 ml of deionized water through sonication at room temperature for 3 hours and then combined with PVA solution. The mixture of PVA and ZrO_2 was stirred for 1 hour and sonicated for 30 minutes. The resulting solution was poured in petri dish and dry at room temperature for two days. The dried composite membrane was peeled off from the Petri dish. We also prepared PVA/ZrO_2 (9 wt%) and PVA/ZrO_2 (13 wt%) composite membranes by repeating same procedure.

2.1.3.4. Preparation of PVA/TiO_2/ZrO_2 composite membranes:

PVA/TiO_2/ZrO_2 composite membranes were synthesized using a simple solution casting technique. To prepare the PVA solution, a known amount (1 g) of PVA was dissolved in 20 ml distilled water and stirred at 80°C until the solution turned transparent. At the same time, to prepare TiO_2 and ZrO_2 solution 0.05 g of each TiO_2 and ZrO_2 nanoparticles were dispersed in 10 ml distilled water in separate beakers by ultra sonication. Then the prepared TiO_2 and ZrO_2 solution were directly mixed with the PVA solution. The mixture was stirred and sonicated for 1 hours to achieve homogeneous dispersion of TiO_2 and ZrO_2
nanoparticles in the PVA and the resulting solution was poured in Petri dish. After drying, obtained uniform ceramic oxides dispersed PVA membranes were removed from the Petri dish.

XRD Characterization:

2.2: XRD Study:

XRD serves as a crucial technique employed to identification of crystalline phases within substances and the measurement of various structural characteristics, such as defect structure, strain, preferred orientation, phase composition, and grain size. Furthermore, XRD is an instrumental technique in finding out the thickness of thin films and multilayers. In the analysis of polymer materials, broad-angle X-ray powder diffraction is commonly employed to acquire valuable information regarding the composition, structural arrangement and condition of the materials. Illustrated in Figure 2.2.1 (a) and (b) are a schematic diagram of the X-ray diffractometer and actual image of XRD instrument (Bruker D8 advanced XRD instrument) used for generating XRD data, which utilizes Cu Kα radiation and λ (wavelength) of 1.54 angstroms.

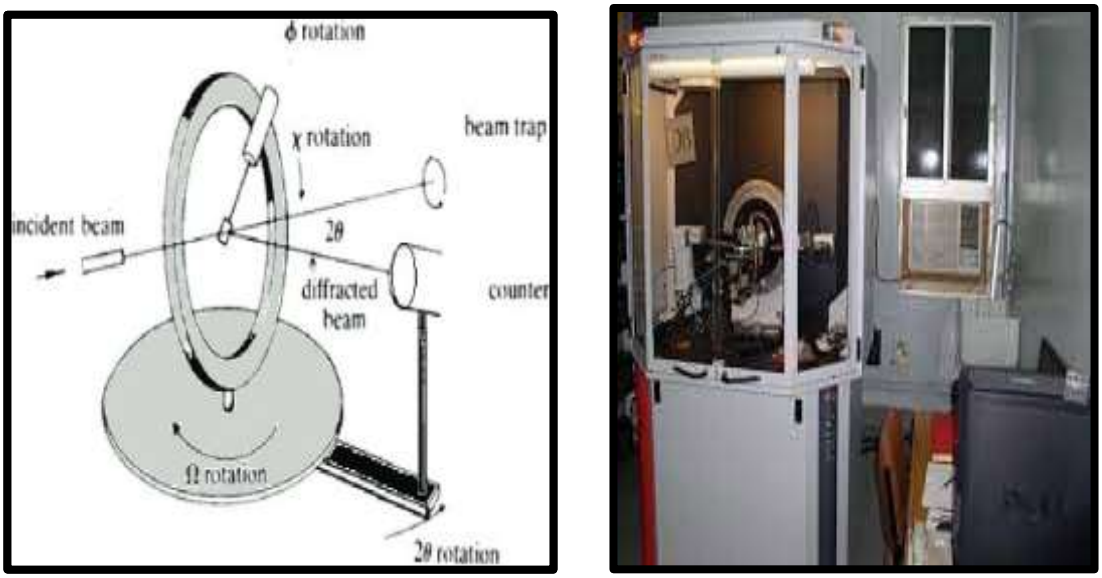

Figure 2.2.1: (a) The model diagram of the XRD [1]. (b) Bruker D8 advanced XRD instrument (UGC-DAE CSR, Indore).

When X-rays scattered by the regular distribution of atoms within a crystal, they undergo a process where both constructive and destructive interference occurs between the scattered rays. This occurs as a result of the X-ray radiation's wavelength and the crystal lattice's scattering centres lengths being on the same order of magnitude. This happens because the distances between the scattering centers in the crystal lattice are similar in magnitude to the X-ray radiation's wavelength. X-rays are effectively "reflected" entirely from the crystal when the angle of incidence of the X-rays fulfilled the Bragg equation:

$$n\lambda = 2d \sin\theta$$

Where θ represents the angle at which the X-ray beam undergoes constructive interference. n denote an integer, d signifies for the crystal's interplanner spacing, and λ for the X-ray's wavelength.

The diffraction patterns of TiO_2 nanoparticles, ZrO_2 nanoparticles, PVA and PVA/composites membranes were recorded at a angle of diffraction 2θ from 10° to 90° at a rate of scanning and step size of 1°/min and 0.05° respectively. Every X-ray experiment was carried out at room temperature.

3:Results and Discussion:

Figure 3.2 illustrates the three distinct crystalline polymorphs of TiO_2 namely brookite anatase, and rutile**.** Each of these structures has a unique atomic arrangement and lattice symmetry. Rutile and Anatase has a tetragonal crystal structure. In the both structures, each titanium (Ti) atom is surrounded by six oxygen atoms, and each oxygen (O) atom bonded with three titanium (Ti) atoms. forming octahedral coordination. In every instance, there exists a slight distortion in the TiO_6 octahedron, where two Ti—O bonds are slightly greater than the remaining four. Furthermore, certain angles of O—Ti—O bond deviate by the

expected 90 degrees. Anatase exhibits a higher distortion compared to rutile. The crystal structures of both rutile and anatase are commonly explained as chains of TiO_6 octahedra with shared edges. Specifically, rutile shares two edges while anatase shares four edges. rutile is the most stable and commonly occurring form of TiO_2 at higher temperatures. Once the formation of the rutile phase occurred, its growth rate notably surpassed that of the anatase phase.

Brookite TiO_2 has an orthorhombic crystal system. Brookite is the least common phase among the three major TiO_2 crystal structures. It is typically found in lower-temperature and high-pressure conditions. The composition of its unit cell consists of eight TiO_2 formula units, which forms through the TiO_6 octahedra that share edge. It possesses greater complexity, exhibits a greater cell volume and being less dense in comparison with two other phases.

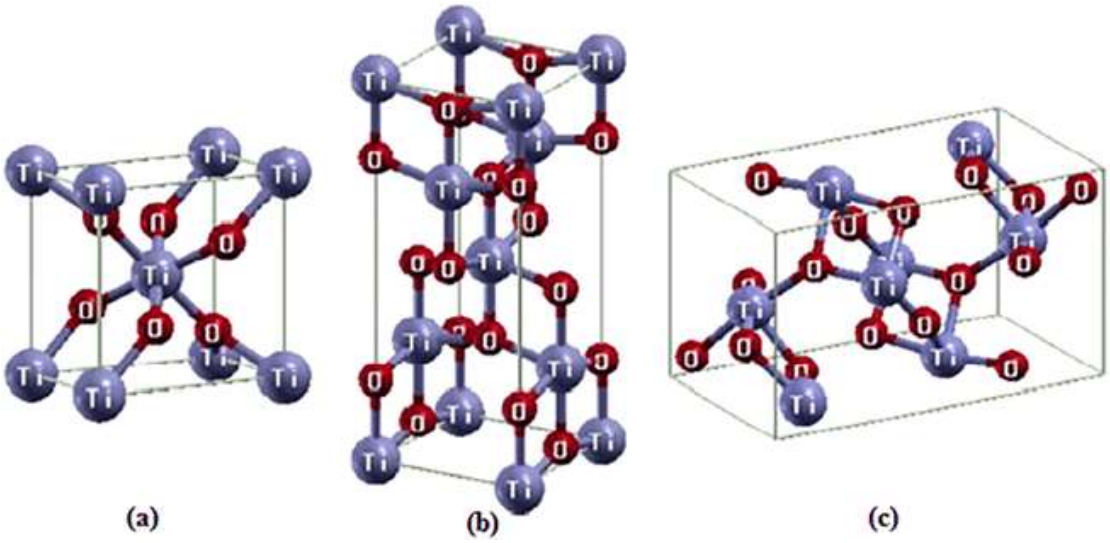

Figure 3.2: TiO_2 crystal structures consisting of (a) anatase, (b) rutile, and (c) brookite [41].

XRD Analysis:

Figure 3.3 illustrates XRD patterns for three TiO_2 nanoparticle samples calcinated at different temperature. The diffraction pattern illustrated in Figure
3.3 (a) exhibits sharp diffraction peaks at 25.19°, 30.35°, 37.24°, 46.72°, 52.76°, 60.29°, 65.88°, 70.84° ,76.66° and 86.22° corresponding to the (120), (121), (201), (032), (240), (123), (161), (332), (024) and (044) plane of TiO_2 brookite
phase with an orthorhombic structure [JCPDS no.29 – 1360].

Figure 3.3 (b) shows sharp diffraction peaks at 25.14°, 27.26°, 35.62°, 37.29°, 38.59°, 40.55°, 43.15°, 46.93°, 52.68° 53.36°, 54.75°, 60.19°, 61.33°, 65.57°, 66.25°,70.50°,71.90°,76.52°, 81.92°, 82.81°, 86.62° and 87.44° which assigned to (120), (110), (101), (201), (211), (022), (210), (032), (240), (320), (211), (123), (052), (221), (161), (332), (311), (024), (321), (333), (044) and (410) plane of brookite – rutile mixed phase respectively (JCPDS no. 29 – 1360 and JCPDS no. 21-1276).

The diffraction pattern illustrated in Figure 3.3 (c) exhibits diffraction peaks at 27.29°, 36.51°, 39.51°, 41.53°, 44.05°, 55.78°, 62.29°, 69.41°, 77.37°,
82.91° and 87.05° corresponding to the (110), (101), (200), (111), (210), (220),
(002), (112), (202), (321) and (410) plane of rutile phase with the tetragonal structure (JCPDS no. 21 - 1276). The Scherrer equation $D = \kappa\lambda / \beta\cos\theta$ has been employed for calculating TiO_2 nanoparticles average grain size. The brookite, brookite-rutile, and rutile phases of TiO_2 were found to have average

sizes of 3.3 nm, 8.4 nm, and 35.7 nm, respectively [42, 43].

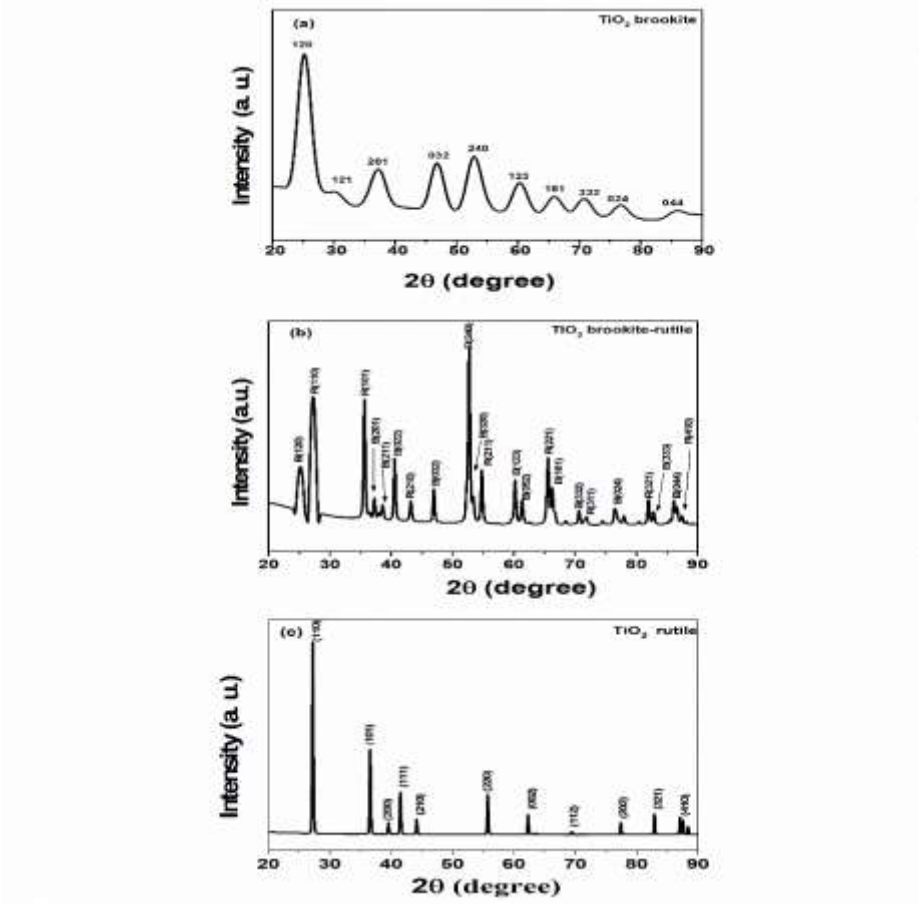

Figure 3.3: XRD pattern for TiO_2 (a) brookite, (b)brookite – rutile and (c) rutile phase.

X-ray diffraction spectra for PVA and PVA/TiO_2 nanocomposite membranes is depicted in Figure 3.4. XRD pattern of PVA membrane [Figure 3.4 (a)] exhibits a diffraction peak at 19.33° corresponds to (101) plane of PVA, which indicating semicrystalline nature of PVA [44]. The XRD pattern of PVA/TiO_2 membrane for three different phases of TiO_2 displayed in Figure 3.4 (b), 3.4 (c), 3.4 (d) exhibited the characteristic diffraction peak of PVA as well as TiO_2. Figure 3 (b) shows the diffraction peaks at 19.25° and 25.15° corresponds to the PVA and TiO_2 brookite phase respectively. Figure 3 (c) shows the diffraction peaks at 19.68°, 25.69°, 27.79° which revealed to the PVA, TiO_2 brookite and TiO_2 rutile phase respectively. In Figure 3 (d) the diffraction peaks were found at 19.30° and 27.30°, 35.96°, 41.09° and 54.37° which revealed the PVA and rutile phase of TiO_2**.** The XRD results of composite membrane reveals TiO_2 nanoparticles became uniformly distributed throughout the PVA matrix. The PVA diffraction peak's intensity increased, indicating that crystallinity of PVA increase with doping of different phases of TiO_2 because it enhances the hydrogen bonds formation among the layers of PVA and causes PVA to crystallize [45]. Additionally, it was shown that the FWHM value of the PVA characteristic diffraction peak decreased as a sequence of PVA/TiO_2 (brookite), PVA/TiO_2 (brookite-rutile) and PVA/ TiO_2 (rutile) composite indicates that PVA/TiO_2 (rutile) composite have a greater degree of crystallinity than other two composites.

For all samples the summary of XRD results have been summarised in the Table 3.1. Doped TiO_2 nanoparticles average size was found to be approximately 3.3 nm, 8.4 nm and 35.7 nm for PVA/TiO_2 (brookite), PVA/TiO_2 (brookite-rutile) and PVA/ TiO_2 (rutile) composite respectively.

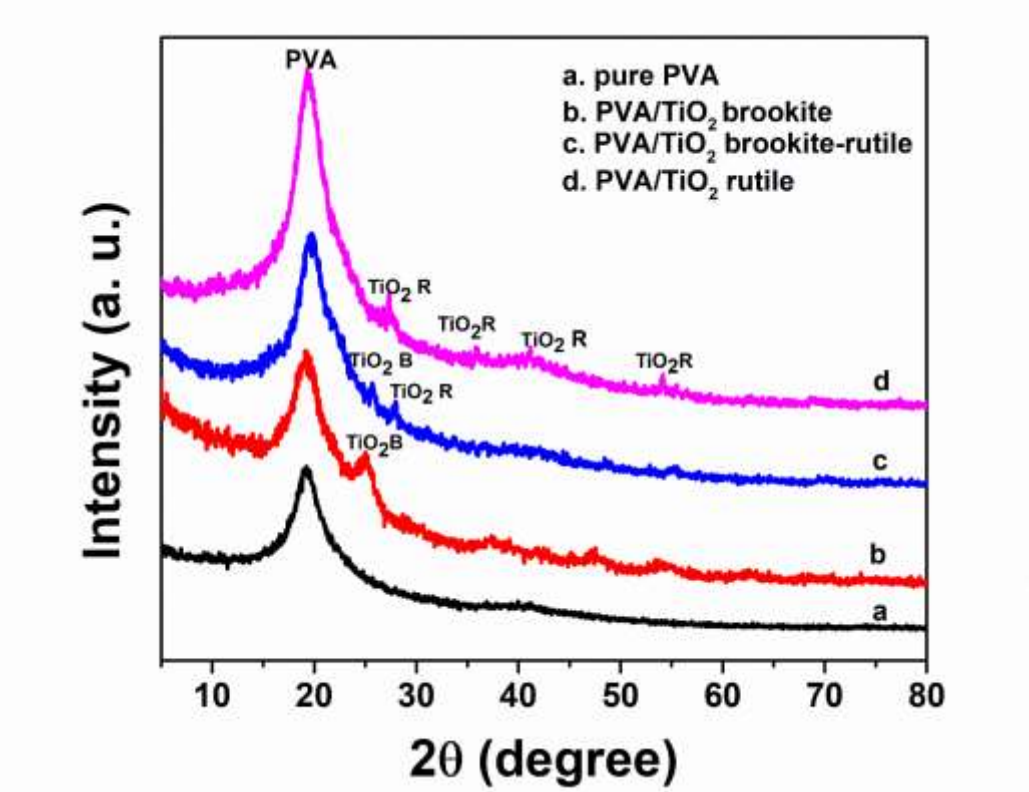

Figure 3.4: X-ray diffraction pattern for PVA and PVA/TiO2 nanocomposite membrane with different TiO2 phases.

Table 3.1: A summary of the observed XRD peak positions, corresponding interplanar spacing, phase assignments and particle size for the different phases of TiO2 nanoparticles, PVA and PVA/TiO2 nanocomposite membrane.

Sample	2θ (degree)	d-values (Å)		Phase assignment	Grain size (nm)
		Obs.	Std.		
TiO2 brookite	25.19	3.53	3.51	Orthorhombic	
	30.35	2.94	2.90		
	37.29	2.41	2.40		
	46.72	1.94	1.96		
	52.76	1.75	1.75		
	60.29	1.53	1.54		
	65.88	1.42	1.41		

	70.84	1.32	1.33		3.3
	76.66	1.24	1.23		
	86.22	1.13	1.12		
TiO_2 brookite-rutile-	25.14	3.58	3.51	Orthorhombic-Tetragonal	8.4
	27.26	3.27	3.24		
	35.62	2.52	2.48		
	37.24	2.41	2.40		
	38.59	2.33	2.33		
	40.55	2.22	2.24		
	43.15	2.09	2.05		
	46.93	1.93	1.96		
	52.68	1.73	1.75		
	53.36	1.71	1.69		
	54.75	1.67	1.68		
	60.19	1.53	1.54		
	61.33	1.50	1.49		
	65.57	1.42	1.42		
	66.25	1.41	1.41		
	70.50	1.32	1.33		
	71.90	1.31	1.30		
	76.52	1.24	1.23		
	81.92	1.17	1.17		
	83.10	1.16	1.15		
	86.62	1.12	1.12		

	87.44	1.11	1.11		
TiO_2 rutile	27.29	3.27	3.24	Tetragonal	35.7
	36.51	2.48	2.48		
	39.51	2.29	2.29		
	41.53	2.17	2.18		
	44.05	2.05	2.05		
	55.78	1.64	1.62		
	62.29	1.48	1.47		
	69.41	1.35	1.34		
	77.37	1.23	1.24		
	82.91	1.16	1.17		
	87.05	1.11	1.11		
PVA	19.33	4.66	4.55		
PVA/TiO_2 Brookite	19.25	4.66	4.55	Orthorhombic	≈ 3.3
	25.15	3.53	3.51		
PVA/TiO_2 brookite – rutile	19.68	4.66	4.55	Tetragonal-Orthorhombic	≈ 8.4
	25.69	3.53	3.51		
	27.79	3.27	3.24		
PVA/TiO_2 rutile	19.30	4.66	4.55	Tetragonal	≈35.7
	27.30	3.27	3.24		
	36.02	2.48	2.48		
	41.09	2.17	2.18		
	54.37	1.64	1.62		

4.1 In pure zirconia, there are three different crystal structures: monoclinic, m- ZrO_2, tetragonal, t- ZrO_2, and cubic, c- ZrO_2.The structure is defined by a unit cell, which is a repeating unit that forms the crystal lattice. Figure 4.1 illustrates the crystal structures of tetragonal ZrO_2. In the tetragonal phase, this unit cell has a rectangular shape, and its dimensions are typically described by two lattice parameters, often denoted as "a" and "c." Zirconium atoms are located at the corners of the rectangular unit cell and form a square lattice along the shorter "a" axis. These Zr atoms are positioned at the vertices of the unit cell.

Oxygen atoms are positioned between the zirconium atoms along the longer "c" axis. In this arrangement, oxygen atoms form layers that separate the layers of zirconium atoms. The oxygen atoms are closely packed in a way that maximizes their interactions with the zirconium atoms. Tetragonal ZrO_2 exhibits
good ionic conductivity, high strength, and fracture toughness [17]. Tetragonal zirconia (t-zirconia) exhibits greater toughness compared to monoclinic (m-) and cubic (c-) ZrO_2, as well as other ceramic materials. Therefore, it serves as a toughening agent for other ceramic materials. These materials are referred to as zirconia toughened ceramics. This structure is closely related to the cubic ZrO_2 structure but differs in two respects, Firstly, In the lattice, there is a distortion, corresponding to a slight c-axis elongation. Secondly, oxygen atom columns are displaced alternately up or down the c axis. As a result, four oxygen neighbours are moved closer to a zirconium atom and the four other oxygen neighbours move away from it. The presence of these interdependent distortions are necessary to prevents O–O contact [18]. Each atom of zirconium maintains its eight-fold coordination with oxygen. It consists of four oxygen atoms at a distance of 2.1 Å atoms, and another four at a distance of 2.3 Å atoms.

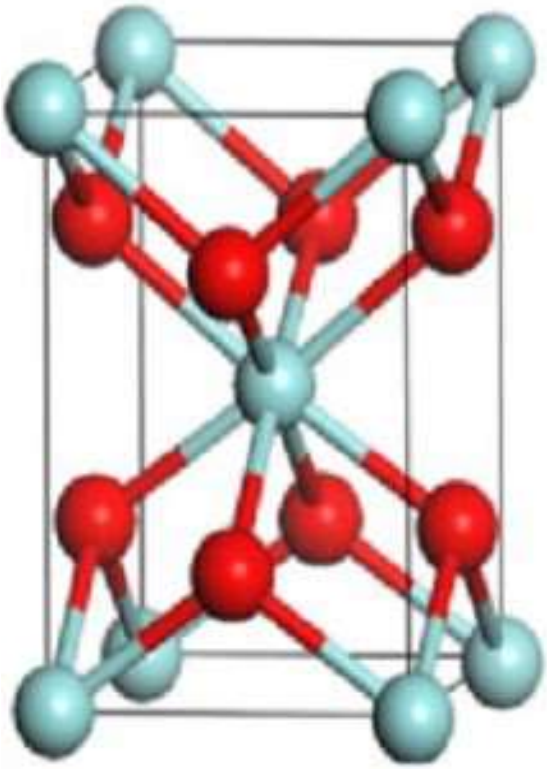

Figure 4.1: Crystal structures of tetragonal ZrO_2, Oxygen and zirconium atoms are represented by red and blue spheres, respectively [19].

XRD Analysis:

The XRD pattern of synthesized ZrO_2 sample calcined at 650°C illustrated in Figure 4.2 (A). All the

prominent peaks are identified according to JCPDS card no. 88-1007. Summary of peak positions, corresponding interplanar spacing, peak intensities, Miller indices and particle size for ZrO_2 nanoparticles are given in Table 4.1. The XRD pattern shows sharp diffraction peaks at $2\theta = 30.24°$, 35°, 50.38°, 60°, 62.90° and 74.38° corresponding to the (101), (110), (112), (211), (202) and (220) planes. ZrO_2 is found to be in the tetragonal phase as indicated by the indexed XRD peaks. The Scherrer's relation, $D = \kappa\lambda\ \beta\cos\theta$ was used to determine the average crystallite size of ZrO_2 nanoparticles, where D is the crystallite size along (hkl) direction, k = 0.9 is the fixed number, β is FWHM of the diffraction peak, λ is the wavelength of X-ray and θ is the Bragg angle [17]. The calculated average value of crystallite size for ZrO_2 nanoparticles was found to be 5.5 nm.

The XRD pattern of pure PVA membrane shown in Figure 4.2 (B). The broad peak observed at $2\theta \approx 19.24°$ which is corresponding to (101) crystal reflection plane of PVA. The new peak observed at 2θ =41.11 corresponds to (202) planes represent the semi-crystalline nature of the PVA and the presence of crystalline and amorphous regions [18, 20].

Figure 4.2 (C) represent the XRD pattern of PVA/ZrO_2 (13 wt%) composite membrane reveals the diffraction peak of both PVA and nanocrystalline ZrO_2. The diffraction peaks at 2θ= 29.59°, 34.23°, 49.40°, 58.75°, 61.40 and 73.23° correspond to the ZrO_2 dopant however the peak located at 18.97° revealed the characteristic diffraction peak of PVA. The diffraction peaks of PVA/ZrO_2 composite membrane shifted to lower angles than that of the pure PVA membrane, which indicates that ZrO_2 nanoparticles has been successfully incorporated into the PVA matrix [21, 22]. Further we noticed that the broadening of characteristic diffraction peak of PVA [for pure PVA at 2θ=19.16°, FWHM =2.93) is decreased in PVA/ZrO_2 composite at position 18.97 (FWHM= 1.79). The results revealed the increased crystallinity of PVA molecular chain in the composite structure. For PVA and PVA/ZrO_2 (13 wt%) composite, observed peak positions, chemical phase and particle size have been summarized in Table 4.2 The particle size of doped ZrO_2 phase, calculated from the FWHM of the prominent peak of ZrO_2 of PVA/ZrO_2 (13 wt%) composite remained unaffected at approximately 5.5 nm.

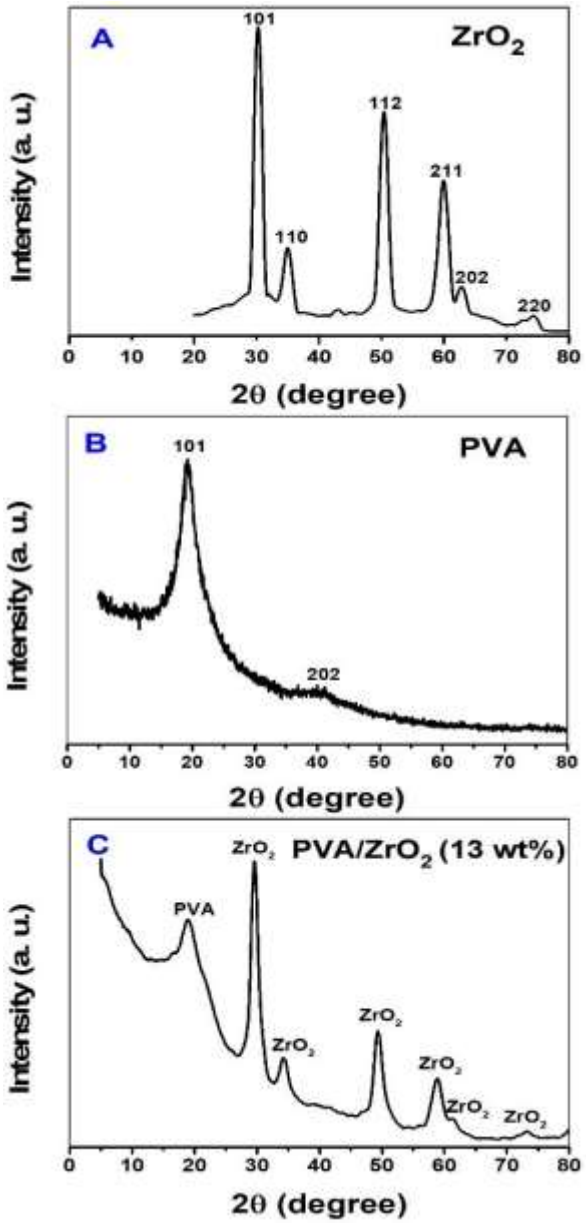

Figure 4.2: X-ray diffraction spectra of (A) ZrO_2 nanoparticles, (B) pure PVA membrane, (C) PVA/ZrO_2 (13 wt%) composite membrane.

Table 4.1: A summary of peak positions, corresponding interplanar spacing, peak intensities, Miller indices and particle size for ZrO_2 nanoparticles.

Sample	2θ (degree)	d-values (Å)		Intensity		Miller indices (hkl)	Particle size (nm)
		Obs.	Std.	Obs.	Std.		
ZrO_2	30.24	2.92	2.95	100	100	(101) [Tetragonal]	5.5
	35	2.56	2.54	29	13.2	(110) [Tetragonal]	
	50.38	1.80	1.81	63	33.6	(112) [Tetragonal]	
	60	1.54	1.53	46	22.6	(211) [Tetragonal]	
	62.90	1.48	1.47	21	5.7	(202) [Tetragonal]	
	74.38	1.28	1.27	13	4.2	(220) [Tetragonal]	

Table 4.2: A summary of peak positions, chemical phase and particle size for PVA and PVA/ZrO_2 (13 wt%) composite membrane.

Sample	2θ (degree)	Chemical phase	Particle size (nm)
PVA	19.24	PVA	5.7 nm
	41.11	PVA	
PVA/ZrO_2 (13 wt%)	18.97	PVA	
	29.59	ZrO_2	
	34.23	ZrO_2	
	49.40	ZrO_2	
	58.75	ZrO_2	
	61.40	ZrO_2	
	73.23	ZrO_2	

The effect of different concentrations of ZrO_2 filler on the optical properties of the PVA/ZrO_2 composites has been studied. The XRD results of the PVA/ZrO_2 composite sample reveal that ZrO_2 nanoparticles were successfully incorporated into PVA matrix and the crystallinity of composite increases with the addition of ZrO_2

References:

[1]. K.S. Hemalatha, K. Rukmani, RSC Adv. 2016, 6, 74354–74366.
[2]. P. L. Reddy, K. Deshmukh, K. Chidambaram, M. M. Nazeer Ali, K. K. Sadasivuni, Y. R. Kumar, R. Lakshmipathy, S. K. Khadheer Pasha, J Mater Sci: Mater Electron. 2019, 30**,** 4676–4687.
[3]. M. Aslam, M. A. Kalyar, Z. A. Raza, Polym. Bull. 2021, 78, 1551–1571.
4]. C. Shao, H.Y. Kim, J. Gong, B. Ding, D. R. Lee, S. J. Park, Mater. Lett. 2003, 57, 1579-1584.
[5]. G. Serdar, Y. Serdar, C. Erdal, A. alicikus, L. Zumre, J. Aust. Ceram. 2018, 54, 523–531.
[6]. S. Mombini, J. Mohammadnejad, B. Bakhshandeh, A. Narmani, J. Nourmohammadi, S. Vahdat, S. Zirak, Int. J. Biol. Macromol. 2019, 140, 278–87.
[7]. S. M. Hwang, J. H. Choi, S. M. Lee, J. H. Lim, J. Joo, J. Phys. Chem. C. 2012, 116, 11386-11392.
[8]. J. Naik, R. F. Bhajantri, V. Hebbaret, S. G. Rathod. Adv Compos Hybrid Mater. 2018, 1, 518–529.
[9]. S. Yoon, T. Noh, W. Kim, J. Choi, H. Lee, Ceram. Int. 2013, 39, 9247–9251.
[10]. S. Lee, H. J. Shin, S. M. Yoon, D. K. Yi, J. Y. Choi, U. Paik, J. Mater. Chem. 2008, 18, 1751–1755.
[11]. T. Wang, Q. Yu, J. Kong, C. Wong, Ceram. Int. 2017, 43, 9296–9302. [12]. M. D. Rhodes, A. T. Bell, J. Catal. 2005, 233, 198–209.
[13]. W. E. Mahmoud, A. A. Al-Ghamdi, Poly. Int. 2010, 59, 1282–1288.

[14]. Z. A. Alrowaili, T. A. Taha, K. S. El-Nasser, H. Donya, J. Inorg. Organomet. Polym. 2021, 31, 3101–3110.
[15]. W. Xiao, J. Song, L. Huang, Z. Yang, Q. Qiao, Ceram. Int. 2020, 46, 29212-29221.
[16]. D. M. Fernandes, A. A. Winkler Hechenleitner, S. M. Lima, L. H. C. Andrade, A. R. L. Caires, E. A. Gómez Pineda, Mater Chem Phys. 2011, 128 371–376.
[17]. A. L. Patterson, Phys. Rev. 1939, 56, 978.
[18]. S. B. Aziz, J. Electron. Mater. 2016, 45 736–745.
[19]. Han, Yong & Zhu, Junfa. (2013). ChemInform Abstract: Surface Science Studies on the Zirconia-Based Model Catalysts. Topics in Catalysis. 56. 10.1007/s11244-013-0156-5.
[20]. O. G. Abdullah, S. A. Saleem, J. Electron. Mater. 2016, 45 5910–5920.
[21]. H. M. Gayitri, M. AL-Gunaid, Siddaramaiah, A. P. Polym. Bull. 2020, 77, 5005–5026.
[22]. C. V. Reddy, I. N. Reddy, J. Shim, D. Kim, K. Yoo, Ceram. Int. 2018, 44, 12329-12339.
[23]. A. F. Mansour, S. F. Mansour, M. A. Abdo, J. Appl. Phys. 2015, 7 60–69.
[24]. M. Aslam, M. A. Kalyar, Z. A. Raza, J. Electron. Mater. 2018, 47, 3912–3926.
[25]. A. Nimrodh Ananth, S. Umapathy, J. Sophia, T. Mathavan, D. Mangalaraj, Appl Nanosci. 2011, 1, 87–96.
[26]. J. Selvi, S. Mahalakshmi, V. Parthasarathy, C. Hu, Y. F. Lin, K. L. Tung, R. Anbarasan, A. A. Annie. Polym. Compos. 2019, 40, 3737-3748.
[27] .S. Akilandeswari, G. Rajesh, D. Govindarajan, K. Thirumalai, M. Swaminathan, J Mater Sci: Mater Electron. 2018, 29, 18258–18270.
[28]. C.V. Reddy, I. N. Reddy, V. V. N. Harish, K. R. Reddy, N. P. Shetti, J. Shim, T. M. Aminabhavi, Chemosphere. 239 (2020) 124766.
[29]. J. Liang, Z. Deng, X. Jiang, F. Li, Y. Li, Inorg. Chem. 2002, 41, 3602–3604.
[30]. K. Smits, D. Jankovica, A. Sarakovskis, D. Millers, Opt. Mater. 2013, 35 462–466.
[31]. A. Arjun, A. Dharr, T. Raguram, K. S. Rajni, J. Inorg. Organomet. Polym. Mater. 2020, 30, 4989–4998.
[32]. S. Ning, P. Zhan, Q. Xie, Z. Li, Z. Appl. Phys. 2013, 46, 445004.
[33]. C. V. Reddy, B. Babu, I. N. Reddy, J. Shim, Ceram Int. 2018, 44, 6940-6948.
[34]. S. Kaci, A. Keffous, A. Kheloufi, I. Bozetine, L. Guerbous, H. Mansouri, Y. Siahmed, S. Bouanik-Aissiou, J. Alloys Compd. 2017, 709, 668–676.
[35]. A. M. Shehapand, D. S. Akil, Int. J. Nanoelectron. Mater. 2016, 9, 17-36. [36]. M. S. P. Shaffer; A. H. Windle, Adv. Mater. 1999, 11, 937–941.
[37]. Z. Cai, R. Remadevi, M. A. A. Faruque, M. Setty, L. Fan, A. N. M. A. Haque, M. Naebe, RSC Adv. 2019, 9, 34076–34085.
[38]. Z Corzo-González, M. I. Loria-Bastarrachea, E. Hernández-Nuñez, M. Aguilar-Vega, M. O. González-Díaz, Polym. Bull. 2017, 74, 2741–2754.
[39]. G. M. Kim, Fabrication of Bio-Nanocomposite Nanofibers Mimicking the Mineralized Hard Tissues via Electrospinning Process. Nanofibers, IntechOpen. London, 2010.
[40]. J. Lee, J. Hong, D. W. Park, S. E. Shim, Opt. Mater. 2010, 32, 530-534.
[41]. G. M. Kim, A. S. Ashraf, G. H. Michler, P. Simon, J. S. Kim, Bioinspir. Biomim. 2008, 3, 046003.
[42]. I. Omkaram, R. P. Sreekanth Chakradhar, J. Lakshmana Rao, Physica B: Condens. Matter, 2007, 388, 318–325.
[43]. E. Al-Emam, H. Soenen, J. Caen, K. Janssens, Herit. Sci. 2020, 8 106.
[44]. A. M. Nawar, A. M. El-Mahalawy, J. Mater. Sci. Mater. Electron. 2020, 31, 3256–3273.
[45]. A. L. Waly, A. M. Abdelghany, A. E. Tarabiah, J. Mater. Res. Technol. 2021, 14, 2962–2969.
[46]. R. N. Oliveira, R. Rouzé, B. Quilty, G. G. Alves, G. D. A. Soares, R. M. S. M. Thiré, G. B. McGuinness, Interface Focus, 2014, 4, 20130049.
[47]. N. Ahad, E. Saion, E. Gharibshahi, J. Nanomater. 2012, 2012, 94–99.